

Discovery of dual “little red dots” indicates excess clustering on kilo-parsec scales

Takumi S. TANAKA,^{1,2,3} John D. SILVERMAN,^{1,2,3,4} Kazuhiro SHIMASAKU,^{2,5} Junya ARITA,² Hollis B. AKINS,⁶ Kohei INAYOSHI,⁷ Xuheng DING,⁸ Masafusa ONOUE,^{1,7} Zhaoxuan LIU,^{1,2,3} Caitlin M. CASEY,^{6,9} Erini LAMBRIDES,¹⁰ Vasily KOKOREV,^{6,11} Shuowen JIN,^{9,12} Andreas L. FAISST,¹³ Nicole DRAKOS,¹⁴ Yue SHEN,^{15,16} Junyao LI,¹⁵ Mingyang ZHUANG,¹⁵ Qinyue FEI,¹⁷ Kei ITO,^{9,12} Wenke REN,^{18,19} Suin MATSUI,² Makoto ANDO,²⁰ Shun HATANO,²¹ Michiko S. FUJII,² Jeyhan S. KARTALTEPE,²² Anton M. KOEKEMOER,²³ Daizhong LIU,²⁴ Henry Joy MCCracken,²⁵ Jason RHODES,²⁶ Brant E. ROBERTSON,²⁷ Maximilien FRANCO,⁶ Irham T. ANDIKA,^{28,29} Aidan P. CLOONAN,³⁰ Xiaohui FAN,³¹ Ghassem GOZALIASL,^{32,33} Santosh HARISH,³⁴ Christopher C. HAYWARD,³⁵ Marc HUERTAS-COMPANY,^{35,36,37,38,39} Darshan KAKKAD,^{23,40} Tomoya KINUGAWA,^{41,42,5} Namrata ROY,⁴ Marko SHUNTOV,^{9,43} Margherita TALIA,^{44,45} Sune TOFT,^{9,43} Aswin P. VIJAYAN,^{9,12} Yiyang ZHANG,⁸

¹Kavli Institute for the Physics and Mathematics of the Universe (WPI), The University of Tokyo Institutes for Advanced Study, The University of Tokyo, Kashiwa, Chiba 277-8583, Japan

²Department of Astronomy, Graduate School of Science, The University of Tokyo, 7-3-1 Hongo, Bunkyo-ku, Tokyo 113-0033, Japan

³Center for Data-Driven Discovery, Kavli IPMU (WPI), UTIAS, The University of Tokyo, Kashiwa, Chiba 277-8583, Japan

⁴Center for Astrophysical Sciences, Department of Physics and Astronomy, Johns Hopkins University, Baltimore, MD 21218, USA

⁵Research Center for the Early Universe, Graduate School of Science, The University of Tokyo, 7-3-1 Hongo, Bunkyo-ku, Tokyo 113-0033, Japan

⁶Department of Astronomy, The University of Texas at Austin, 2515 Speedway Boulevard Stop C1400, Austin, TX 78712, USA

⁷Kavli Institute for Astronomy and Astrophysics, Peking University, Beijing 100871, China

⁸School of Physics and Technology, Wuhan University, Wuhan 430072, China

⁹Cosmic Dawn Center (DAWN), Denmark

¹⁰NASA-Goddard Space Flight Center, Code 662, Greenbelt, MD, 20771, USA

¹¹Kapteyn Astronomical Institute, University of Groningen, 9700 AV Groningen, The Netherlands

¹²DTU Space, Technical University of Denmark, Elektrovej, Building 328, 2800, Kgs. Lyngby, Denmark

¹³Caltech/IPAC, 1200 E. California Blvd. Pasadena, CA 91125, USA

¹⁴Department of Physics and Astronomy, University of Hawaii, Hilo, 200 W Kawili St., Hilo, HI 96720, USA

¹⁵Department of Astronomy, University of Illinois at Urbana-Champaign, Urbana, IL 61801, USA

¹⁶National Center for Supercomputing Applications, University of Illinois at Urbana-Champaign, Urbana, IL 61801, USA

¹⁷Department of Astronomy, School of Physics, Peking University, Beijing 100871, China

¹⁸CAS Key Laboratory for Research in Galaxies and Cosmology, Department of Astronomy, University of Science and Technology of China, Hefei, Anhui 230026, People's Republic of China

¹⁹School of Astronomy and Space Science, University of Science and Technology of China, Hefei 230026, People's Republic of China

²⁰National Astronomical Observatory of Japan, 2-21-1 Osawa, Mitaka, Tokyo, 181-8588, Japan

²¹Department of Astronomical Science, SOKENDAI (The Graduate University for Advanced Studies), Osawa 2-21-1, Mitaka, Tokyo, 181-8588, Japan

²²Laboratory for Multiwavelength Astrophysics, School of Physics and Astronomy, Rochester Institute of Technology, 84 Lomb Memorial Drive, Rochester, NY 14623, USA

²³Space Telescope Science Institute, 3700 San Martin Drive, Baltimore, MD 21218, USA

²⁴Purple Mountain Observatory, Chinese Academy of Sciences, 10 Yuanhua Road, Nanjing 210023, China

²⁵Institut d'Astrophysique de Paris, UMR 7095, CNRS, and Sorbonne Université, 98 bis boulevard Arago, 75014 Paris, France

²⁶Jet Propulsion Laboratory, California Institute of Technology, 4800 Oak Grove Drive, Pasadena, CA 91001, USA

²⁷Department of Astronomy and Astrophysics, University of California, Santa Cruz, 1156 High Street, Santa Cruz, CA 95064, USA

²⁸Technical University of Munich, TUM School of Natural Sciences, Department of Physics, James-Franck-Str. 1, 85748 Garching, Germany

²⁹Max-Planck-Institut für Astrophysik, Karl-Schwarzschild-Str. 1, 85748 Garching, Germany

³⁰Department of Astronomy, University of Massachusetts, 710 North Pleasant Street, Amherst, MA 01003, USA

³¹Steward Observatory, University of Arizona, 933 N. Cherry Ave., Tucson, AZ 85721, USA

³²Department of Computer Science, Aalto University, PO Box 15400, Espoo, FI-00 076, Finland

³³Department of Physics, Faculty of Science, University of Helsinki, 00014-Helsinki, Finland

³⁴Laboratory for Multiwavelength Astrophysics, School of Physics and Astronomy, Rochester Institute of Technology, 84 Lomb Memorial Drive, Rochester, NY14623, USA

³⁵Center for Computational Astrophysics, Flatiron Institute, 162 Fifth Avenue, New York, NY 10010, USA

³⁶Instituto de Astrofísica de Canarias (IAC), La Laguna 38205, Spain

³⁷Observatoire de Paris, LERMA, PSL University, 61 avenue de l'Observatoire, 75014 Paris, France

³⁸Université Paris-Cité, 5 rue Thomas Mann, 75014 Paris, France

³⁹Universidad de La Laguna, Avda. Astrofísico Fco. Sanchez, La Laguna, Tenerife, Spain

⁴⁰Centre for Astrophysics Research, University of Hertfordshire, Hatfield, AL10 9AB, UK

⁴¹Faculty of Engineering, Shinshu University, 4-17-1, Wakasato, Nagano-shi, Nagano 380-8553, Japan

⁴²Research Center for Aerospace System, Shinshu University, 4-17-1, Wakasato, Nagano-shi, Nagano 380-8553, Japan

⁴³Niels Bohr Institute, University of Copenhagen, Jagtvej 128, DK-2200 Copenhagen N, Denmark

⁴⁴University of Bologna, Department of Physics and Astronomy (DIFA), Via Gobetti 93/2, I-40129, Bologna, Italy

⁴⁵INAF – Osservatorio di Astrofisica e Scienza dello Spazio, via Gobetti 93/3 - 40129, Bologna - Italy

*E-mail: takumi.tanaka@ipmu.jp

Abstract

“Little Red Dots” (LRDs) are an abundant high-redshift population newly discovered by the James Webb Space Telescope (JWST). They are characterized by a red color in the rest-frame optical band, compact morphology, and broad Balmer emission lines ($\text{FWHM} \gtrsim 1000 \text{ km s}^{-1}$) that suggest an AGN nature. Using a method of pixel-by-pixel color selection and relaxing the compactness criteria, we identify three of the first dual LRD candidates in the COSMOS-Web survey with projected separations of $0''.2\text{--}0''.4$ (1–2 pkpc at their photometric redshifts). A comparison between existing LRD samples and mock data reveals that the projected separations of these dual LRD candidates are unlikely to result from chance projections of objects at different redshifts. In one case (CW-B5-15958), the dual LRD includes two bright sources ($m_{\text{F444W}} = 24.3$ and 24.8) with characteristic V-shape spectral energy distribution (SEDs) and photometric redshifts consistent with each other. We find that CW-B5-15958 has a faint off-centered component and a companion galaxy. In the other two dual systems, the brighter LRD exhibits a V-shape SED, while the fainter LRD ($m_{\text{F444W}} \gtrsim 26$) is undetected in both F115W and F150W. These discoveries suggest that the angular auto-correlation function (ACF) of LRDs exhibits a significant excess ($\sim 3 \times 10^2$ times) on sub-arcsec (kilo-parsec) separations compared to the extrapolation of a power-law ACF of JWST-found AGNs measured over $10''\text{--}100''$. Follow-up spectroscopic confirmation of their redshifts and the construction of a larger sample are essential to advance our understanding of the evolution of supermassive black holes and the importance of mergers in the early universe.

Keywords: galaxies: evolution, quasars: supermassive black holes, galaxies: active, galaxies: high-redshift, galaxies: interactions

1 Introduction

Supermassive black holes (SMBHs) are a key component in the galaxy evolution scenario. The tight relation between black hole mass (M_{BH}) and galaxy properties, such as stellar velocity dispersion, bulge mass, and stellar mass (M_*), observed in the local universe (e.g., Magorrian et al. 1998; Ferrarese & Merritt 2000; Marconi & Hunt 2003; Häring & Rix 2004; Gültekin et al. 2009; Graham et al. 2011; Beifiori et al. 2012; Kormendy & Ho 2013; Reines & Volonteri 2015), implies that SMBHs influence star formation in galaxies through feedback from active galactic nucleus (AGN) activity (AGN feedback, e.g., Springel et al. 2005; Di Matteo et al. 2008; Hopkins et al. 2008; Fabian 2012; DeGraf et al. 2015; Harrison 2017).

The James Webb Space Telescope (JWST), with deep observations at infrared wavelengths, has enabled the discovery of high- z low-luminosity AGNs, thus expanding the parameter space and reducing observational biases in the studies of the evolution of SMBHs and their relationship to their host galaxies. In addition to searches using color selection from photometric data (e.g., Onoue et al. 2023; Labbé et al. 2023; Furtak et al. 2023; Barro et al. 2024; Kokorev et al. 2024), deep near-infrared spectroscopic observations have identified numerous type-I (e.g., Kocevski et al. 2023; Harikane et al. 2023; Maiolino et al. 2023a; Matthee et al. 2024a) and type-II (Scholtz et al. 2023) low-luminosity AGNs ($M_{\text{UV}} \gtrsim -23$).

One of the surprising discoveries with JWST is a new population, named “little red dots” (LRDs, Matthee et al. 2024a), char-

acterized by compact morphologies and V-shape SEDs: blue excess in the rest-UV wavelengths and red color in the rest-optical wavelengths (e.g., Labbé et al. 2023; Furtak et al. 2024; Matthee et al. 2024a; Kocevski et al. 2023; Akins et al. 2023; Barro et al. 2024; Akins et al. 2024b). Spectroscopic observations find broad Balmer lines with the full width at half maximum (FWHM) of $\gtrsim 1000 \text{ km s}^{-1}$, suggesting that LRDs are type-I AGNs (e.g., Labbe et al. 2023; Furtak et al. 2024; Matthee et al. 2024a; Greene et al. 2024; Akins et al. 2024a). Their BH mass (M_{BH}) is typically found to be $\gtrsim 10^7 M_{\odot}$ under the assumption that broad emission lines are attributed to type-I AGNs¹. Some studies have also reported the possibility that LRDs are super-Eddington SMBHs (e.g., Greene et al. 2024; Lambrides et al. 2024; Inayoshi & Maiolino 2024; Inayoshi et al. 2024; Mazzolari et al. 2024). However, with the non- or tentative-detection of X-ray (Maiolino et al. 2024; Ananna et al. 2024; Yue et al. 2024; Akins et al. 2024b), infrared emission from hot torus (Pérez-González et al. 2024; Akins et al. 2024b; Casey et al. 2024), radio (Akins et al. 2024b; Perger et al. 2024; Mazzolari et al. 2024), and variability (Kokubo & Harikane 2024; Zhang et al. 2024; Tee et al. 2024), the possibility that LRDs are not AGNs is still left open.

The cosmic abundance of LRDs is 1–2 dex higher (Kokorev et al. 2024; Kocevski et al. 2024; Akins et al. 2024b) than the extrapolation from the luminosity functions of the high- z luminous quasars (Matsuoka et al. 2016; Niida et al. 2020). The abun-

¹ Note that Lambrides et al. (2024) suggests that $M_{\text{BH}} \lesssim 10^{6-6.5} M_{\odot}$ based on the constraints for the X-ray power slope, Γ , instead of using broad lines.

dant LRD population can be a key building block of the early SMBHs. To explain the rapid formation of a high- z SMBHs, several theoretical studies before JWST proposed mechanisms such as super-Eddington accretion and massive seed BHs, including direct collapse BHs (e.g., Haehnelt & Rees 1993; Loeb & Rasio 1994; Bromm & Loeb 2003; Begelman et al. 2006; Omukai et al. 2008; Alexander & Natarajan 2014; Bhowmick et al. 2022; Zhu et al. 2022). JWST observations have also provided evidence supporting these scenarios (e.g., Maiolino et al. 2023b; Kokorev et al. 2023; Bogdán et al. 2024; Lambrides et al. 2024; Inayoshi & Maiolino 2024; Tripodi et al. 2024).

BH mergers represent another possible mechanism for promoting rapid growth (Yu & Tremaine 2002; Capelo et al. 2015; Liu & Inayoshi 2024). An assessment of their impact requires constraining the merger rate through observations and comparing with theoretical studies (e.g., Liu & Inayoshi 2024). In fact, theoretical efforts (e.g., Volonteri et al. 2022; Chen et al. 2023; Byrne-Mamahit et al. 2024) and observational studies (e.g., Alonso et al. 2007; Woods & Geller 2007; Koss et al. 2010; Ellison et al. 2011; Silverman et al. 2011; Weston et al. 2017; Goulding et al. 2018; Ellison et al. 2019; Perna et al. 2023a; Steffen et al. 2023; Bickley et al. 2024; Comerford et al. 2024; La Marca et al. 2024; Ellison et al. 2024; Uematsu et al. 2024) demonstrate that mergers and interactions trigger AGNs by efficiently supplying fuel to the central regions of galaxies. Furthermore, accurate measurements of the merger rate at early cosmic epochs will also improve our understanding of the prospects of detecting gravitational waves from distant BH mergers (e.g., De Rosa et al. 2019; Goulding et al. 2019; Barausse et al. 2020) in future observations, such as the Laser Interferometer Space Antenna (LISA, Amaro-Seoane et al. 2017).

Previous studies with JWST have explored dual AGNs and close pairs of AGNs at the same redshift from 1D spectra (Maiolino et al. 2023a), images (Harikane et al. 2024; Li et al. 2024), and integral field unit (IFU) spectra (Perna et al. 2023b, 2023a; Übler et al. 2024; Ishikawa et al. 2024; Zamora et al. 2024). While these studies show that there are many merging AGNs in the high- z universe with a fraction of roughly 10-30% (Li et al. 2024; Perna et al. 2023a), dual LRDs have yet to be discovered. One possible reason may be that the photometric selection of LRDs in previous studies uses aperture (or total) color and compactness to identify high- z LRD candidates. The most widely used color criteria is $m_{F277W} - m_{F444W} > 1.5$ (e.g., Barro et al. 2024; Akins et al. 2024b) for selecting objects with a red color. To constrain the compactness, some studies (e.g., Greene et al. 2024; Akins et al. 2024b) use the ratio of aperture fluxes with different diameters. For example, Akins et al. (2024b) uses the aperture photometry of F444W with $0''.2$ and $0''.5$ diameters and selects compact objects with a flux ratio of $F_{F444W}(0''.2)/F_{F444W}(0''.5) > 0.5$. These selection methods may overlook LRDs with nearby components since very close companions with projected separation of $\theta \lesssim 0''.5$ (correspond to $\lesssim 2-3$ kpc at $z \sim 5-7$) can lead to an underestimation of the compactness or incorrect assessment of their color (particularly in cases where the companions are bluer than the LRDs; see Tanaka et al. 2024 for an example). Therefore, this approach would, as intended, favor the selection of isolated “dot”-like objects and overlook LRDs without nearby components.

Here, we develop a pixel-by-pixel color selection method to address this “dots” bias. This paper focuses on the first dual LRD candidates discovered from objects selected with the pixel-by-pixel color selection method (Tanaka et al. 2024; Tanaka et al. in preparation). In this paper, we introduce the data and selection

methods in section 2. In section 3, we introduce the first dual LRD candidates. Based on these results, section 4 discusses the number density of dual LRDs to constrain the nature of LRDs and provide the prospects for the selection of LRDs. Throughout this paper, the AB magnitude system (Oke & Gunn 1983) was adopted, assuming a Kroupa (2001) initial mass function and a standard cosmology with $H_0 = 70 \text{ km s}^{-1} \text{ Mpc}^{-1}$, $\Omega_m = 0.30$, and $\Omega_\Lambda = 0.70$. All separations are given in physical (not comoving) units.

2 Methods

2.1 Data

To conduct a comprehensive LRDs search, we use the JWST images from COSMOS-Web (Casey et al. 2023), which is a Cycle 1 JWST treasury survey program covering an area of 0.54 deg^2 with NIRCam (Rieke et al. 2023; F115W, F150W, F277W, F444W) and 0.19 deg^2 with MIRI (Bouchet et al. 2015; F770W). The data are reduced with the JWST Calibration Pipeline² (Bushouse et al. 2023) version 1.14.0 and the calibration Reference Data System version 1223. The final pixel scale is $0''.030/\text{pixel}$ (see Franco et al., in preparation for details of the data reduction process). The 5σ depths in a $0''.15$ radius aperture range between 26.7 to 27.5 mag in F115W and 27.5 to 28.2 mag in F444W (see Section 2.1 of Casey et al. 2023). In addition, we use the Hubble Space Telescope/ACS F814W data (Koekemoer et al. 2007).

2.2 Identification of dual LRD candidates

We apply a color selection to each pixel (i.e., a pixel-by-pixel color selection method) instead of using aperture or total photometry. The full details of the selection method and subsequent catalog will be presented in a future effort (Tanaka et al. in preparation). Here, we briefly describe the selection method.

First, we perform a pre-selection to limit the parent sample to objects with a high signal-to-noise ratio (S/N) for a robust color estimate in each pixel. We run SExtractor (Bertin & Arnouts 1996) on the NIRCam F444W images to perform source detection and simple aperture photometry with a diameter of $0''.5$. Based on the photometric catalog, we limit our sample to objects detected in F444W with $S/N > 14$, following Greene et al. (2024). Note that the pre-selected sample is free from a bias to compact objects since it relies solely on S/N in single aperture photometry and not on compactness.

For then assessing the color of each pixel, we use a point spread function (PSF) modeled with PSFEx (Bertin 2011) for each filter and match the PSFs of all images to that of F444W with the FWHM of $\sim 0''.16$, which has the largest PSF of the COSMOS-Web NIRCam images. We then create cutout images of 67 pixels square ($\sim 2''.0$) for the pre-selected objects.

Next, we generate a S/N map for each filter and a $m_{F277W} - m_{F444W}$ color map for each cutout image. From the S/N and color maps, we generate a mask image to extract the region with at least ten contiguous pixels having a color of $m_{F277W} - m_{F444W} > 1.5$ (e.g., Barro et al. 2024; Akins et al. 2024b) and a signal-to-noise ratio $S/N > 2$ in each pixel for both the F277W and F444W images.

Since we do not require any upper limit on the size of contiguous regions that pass the color selection criteria, the selected objects include red (possibly dust-obscured) extended galaxies without a PSF-like component (e.g., Gentile et al. 2024). To separate

² <https://github.com/spacetelescope/jwst>

the sample into normal dusty galaxies and objects with an unresolved PSF component (possibly AGN or LRDs), we conduct 2D image modeling on the F444W cutout images, where LRD-like-color unresolved components should have a strong contribution to the total flux.

Then, we utilize the 2D image modeling tool `galight` (Ding et al. 2020) and perform the fitting of each cutout image with three different models: single PSF, Sérsic (Sérsic 1963; Sérsic 1968), and PSF+Sérsic composite models. In the Sérsic and PSF+Sérsic models, we first perform the segmentation using the `detect_obj` function in `galight`. This function performs automatic segmentation on regions with $> 3\sigma$ pixels (`n_sigma=3`) that extend over more than 7 pixels (`n_pixels=7`). Then, we assign each segmented region as a Sérsic component in the fittings. To separate the extended components from PSF components, we set the range of effective radius r_e and Sérsic index n as $[0''.1, 2''.0]$ and $[0.5, 5.0]$, respectively. With the fitted results, we select objects where the Bayesian Information Criterion (BIC) for the single PSF or PSF+Sérsic model is significantly lower³ than the BIC for the Sérsic-only model, i.e., we select objects to have at least a PSF-like core.

For quality assurance, we check the cutout images of stars (i.e., expected to be a PSF) and confirm that the center of the PSF components in different filters are well aligned. Thus, there is no significant spatial offset among different filter images that affect the color of each pixel.

The selected sample includes dusty AGNs with host galaxies, X-ray and radio detections (Tanaka et al. 2024; Tanaka et al. in preparation), and LRDs. We confirm that our method selects typical LRDs with $m_{F444W} \lesssim 25$ at high completeness and also overlooked LRDs, e.g., those with close companions (see Tanaka et al. in preparation). Among these objects, we identify three of the first dual LRD candidates, where two compact sources with colors similar to LRDs are located within a $2'' \times 2''$ cutout field, separated by $0''.2\text{--}0''.4$. These candidates are described in detail in section 3. Interestingly, from the selected sample, we cannot find any other dual LRD candidates with separations of $\lesssim 1''$, i.e., LRDs with companion LRDs within the cutout image. Again, this paper only focuses on these three newly-discovered dual LRD candidates. The details of the pixel-by-pixel color selection method and the full sample will be presented in following papers (Tanaka et al. in preparation).

3 Results: dual LRD candidates

From the full sample selected by the method described above, we identify three dual LRD candidates within the COSMOS-Web field where two red, unresolved objects are at close separation ($\theta = 0''.2\text{--}0''.4$) as shown in figure 1. The probability of observing LRD pairs with $\theta \sim 0''.4$ due to a chance projection of foreground/background LRDs is extremely low, as demonstrated in section 4.1. Throughout the paper, the brighter LRD in each pair is referred to as component #1 while the fainter LRD is referred as component #2.

We also apply the same selection method to the image data from JADES and CEERS, and do not find similar dual LRD candidates. The area covered by COSMOS-Web (0.54 deg^2) is approximately ~ 20 and ~ 11 times larger than CEERS ($\sim 100 \text{ arcmin}^2$) and JADES (175 arcmin^2), respectively. Therefore, the difference in

the survey area is consistent with the number of dual LRD candidates found in COSMOS-Web and not present in CEERS and JADES. However, as discussed in section 2 and at the end of this section, there remains a possibility that our method can select bright ($m_{F444W} \lesssim 25$) LRDs, i.e., we could overlook fainter dual LRDs in these fields.

To measure the photometry of each LRD within these systems, we perform image-based modeling using `galight` (Ding et al. 2020). We simultaneously fit each component with either a Sérsic profile (Sérsic 1963; Sérsic 1968) or a PSF to check whether spatially unresolved components describe these candidates or not. Therefore, the number of fitted models is four: Sérsic-Sérsic, Sérsic-PSF, PSF-Sérsic, and PSF-PSF for the pair of LRD candidates. The center position of each component is fixed based on the PSF-PSF fitting results for F444W. For F115W and F150W of CW-A6-19978 and CW-B2-4383, we also test a case where we do not apply a model to component #2, i.e., undetected in these filters. We determine whether each component is best represented by a PSF or an extended Sérsic profile using the BIC. When fitting with Sérsic components, we set the r_e and n ranges to $[0''.03, 1''.0]$ and $[0.5, 5.0]$, respectively, to separate the extended components from PSF components effectively. Using the best model chosen based on the BIC, we measure the photometry of each component as summarized in table 1.

To estimate photometric redshifts (z_{photo}), we also perform SED fitting analysis using a flexible type-I AGN template capable of describing the SEDs of LRDs, following the methodology of Akins et al. (2024b). Below, we provide an overview of the approach and refer the reader to section 3.4.1 of Akins et al. (2024b) for the detailed procedures. For the accretion disk continuum, we assume a single power-law model, $F_\lambda \propto \lambda^{\beta_s}$, with two free parameters: the spectral slope β_s and the intrinsic UV magnitude (scaling parameter). We use the QSO emission line template from Temple et al. (2021) (`emline_type=0`) with adjustments to reconstruct the high-EW broad emission lines (Akins et al. 2024b). For dust attenuation, we use the empirical quasar attenuation law from Temple et al. (2021). Additionally, we include a scattering component of the AGN intrinsic SED to describe blue excess at rest-UV wavelengths. The model is fit to the data using the `MultiNest` nested sampling algorithm. The best-fit model SEDs are shown by solid lines in figure 2. The properties of each LRD determined through these analyses are summarized in table 1.

Our understanding of the SEDs of LRDs is still uncertain, particularly the strength of the galaxy and AGN contributions to each SED component. This SED fitting is an extreme case where we assume that the SEDs are only composed of AGN components; therefore, we only use the estimated value of z_{photo} in this paper and not the other SED parameters. For component #2 in CW-A6-19978 and CW-B2-4383, which are only detected at longer wavelengths (F277W, F444W, and F770W), we use upper limits to the photometry for the F115W and F150W filters.

In addition to SED fitting with a QSO model, we also use brown dwarfs (BDs) templates to remove their potential contamination following the method in Akins et al. (2024b). We construct a comprehensive grid of models spanning a broad parameter space. We include three models: cloudy-atmosphere models in chemical equilibrium (Sonora-Diamondback; $T \sim 900\text{--}2400 \text{ K}$; Morley et al. 2024), cloud-free models in chemical equilibrium (Sonora-Bobcat; $T \sim 200\text{--}1300 \text{ K}$; Marley et al. 2021) and disequilibrium (ElfOwl; $T \sim 300\text{--}1000 \text{ K}$; Mukherjee et al. 2024), and low-metallicity models (LOWZ; $[M/H] = -1$; Meisner et al. 2021). The grid explores a range of temperatures ($T = 200\text{--}2400 \text{ K}$), sur-

³ In this study, we use “significantly lower” BIC for cases where the BIC is lower by more than 10 than the other models.

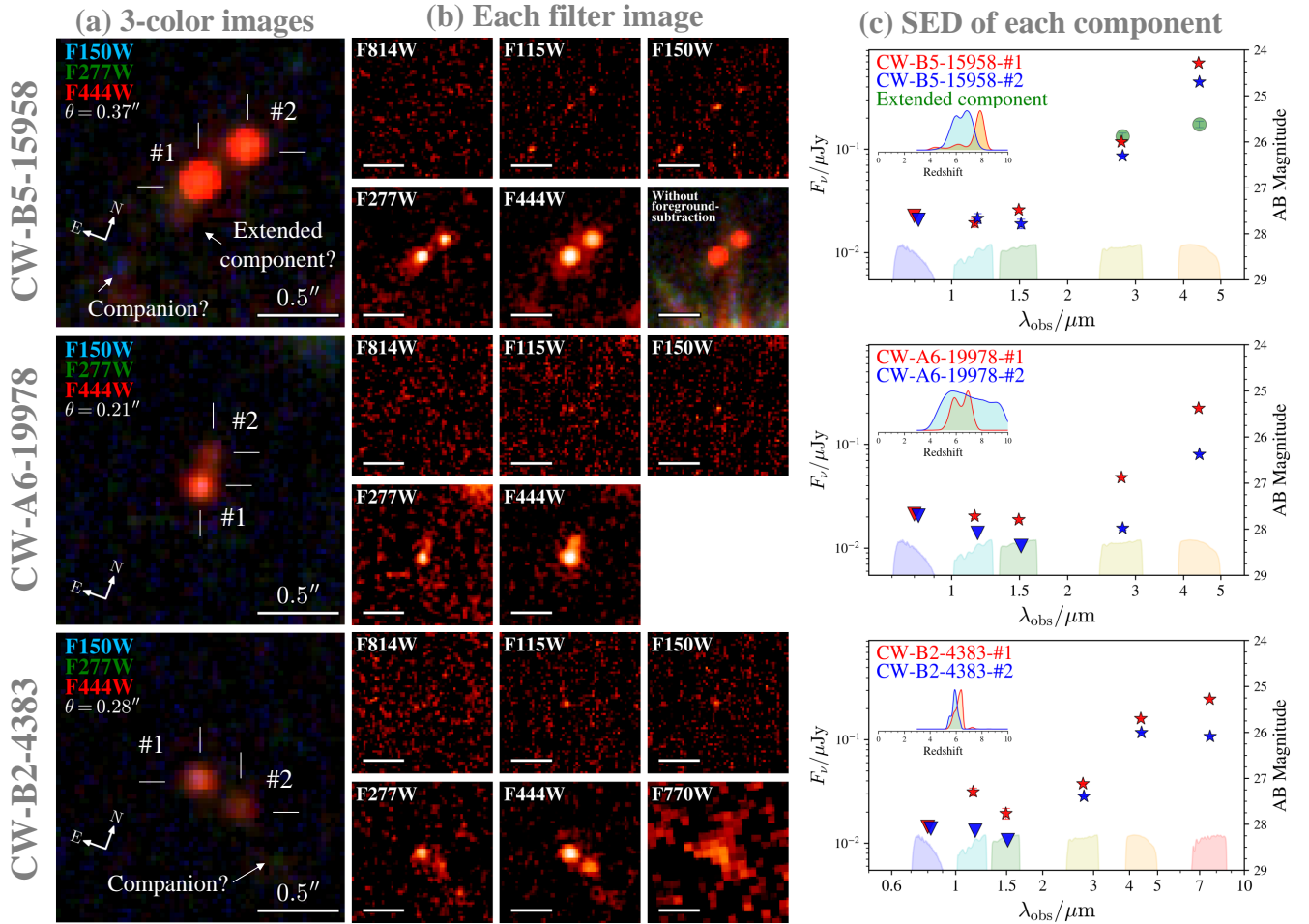


Fig. 1. (a) Three-color (F444W, F277W, and F150W for RGB) image of each dual LRD candidate. We have not matched the PSF between each filter. For CW-B5-15958, we plot the images after subtracting the foreground type-1 AGN (CID-643; see section 3.1). (b) Individual HST (ACS: F814W) and JWST images (NIRCam: F115W, F150W, F277W, and F444W, MIRI: F770W). For CW-B5-15958, we also display the original three-color image before subtracting the foreground type-1 AGN. (c) SED of each component estimated from an imaged-based modeling analysis with probability distributions of z_{photo} . The inverted triangles indicate the 3σ upper limits due to non-detections in specific filters. The best-fit model SEDs are shown in figure 2.

face gravities ($g \sim 100\text{--}3160 \text{ cm s}^{-2}$), and metallicities ($[M/H] = -1, -0.5, \text{ and } 0$). We compare the χ^2 of the best-fit BD templates with χ^2 of the best-fit QSO model. The best-fit model SEDs are shown in dashed lines in figure 2. The χ^2 with the QSO model are significantly lower than those for the BD fits, and the BD templates are inconsistent with the observed photometry. Therefore, we conclude that these objects are not BDs. Detailed analysis and discussion of each candidate are described in the following subsections.

3.1 CW-B5-15958

CW-B5-15958 is located $1''.8$ away from an X-ray-detected AGN at $z_{\text{spec}} = 2.03$, CID-643, whose PSF component impacts the emission from CW-B5-15958 as shown in the bottom-right panel of figure 1 (b) and figure 3 (a). Therefore, before performing image-based modeling of CW-B5-15958, we first subtracted the contribution of CID-643 from the original images. In this step, we model CID-643 with a composite model of a PSF component representing the AGN and a Sérsic component for the host galaxy. For F277W and F444W, we also add two PSF components at the po-

sition of CW-B5-15958 to prevent its influence on the CID-643 modeling. Figure 3 (a) displays this subtraction analysis, where the residual images show the noise-scaled image after subtracting only the CID-643 components, i.e., CW-B5-15958 components are not subtracted even though they are simultaneously modeled in F277W and F444W, suggesting that the foreground contamination are effectively removed from the original images.

Next, we perform image-based modeling on the foreground subtracted images following the same procedure used for other objects (figure 3 (b)). In all filters, both components are better described by PSFs rather than Sérsic profiles. The $m_{F277W} - m_{F444W}$ colors for components #1 and #2 are 1.9 and 1.8, respectively. The optical slopes β_{opt} , estimated from F444W and F277W, are $\beta_{\text{opt}} = 1.75 \pm 0.02$ and 1.52 ± 0.02 for components #1 and #2, respectively, similar to the slopes observed in typical LRDs (Matthee et al. 2024a; Greene et al. 2024; Kocevski et al. 2024). Additionally, components #1 and #2 have $m_{F115W} - m_{F150W}$ colors of 0.3 and -0.1 , indicating a blue excess. These color differences suggest that components #1 and #2 are not gravitationally lensed images of the same object. Both SEDs exhibit an LRD-like V-shape, and fitting with the QSO model yields a lower χ^2 than BD templates.

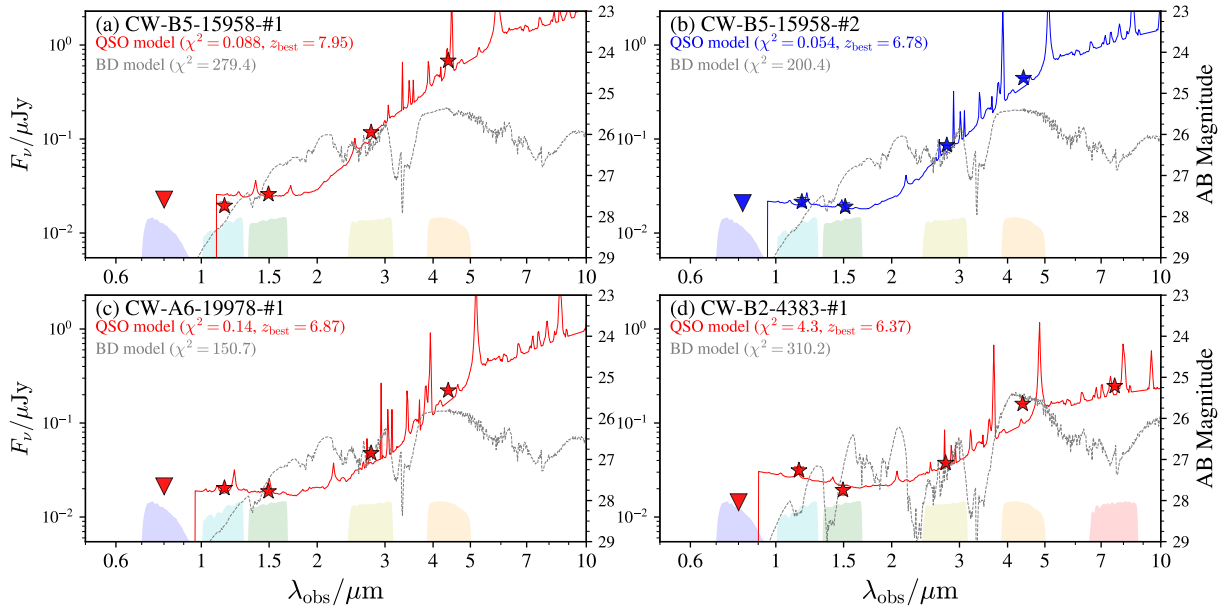


Fig. 2. SED fitting analysis of the LRD candidates with detection in shorter bands (F115W and F150W). The inverted triangle symbols indicate the 3σ upper limit due to the non-detection in each filter. Solid colored and dashed gray lines indicate the best-fit model SEDs with the QSO models and the BD templates. The χ^2 and the best-fit z_{photo} are shown in the upper left corner.

Table 1. Properties of each dual LRD candidate

	R.A. ^a [deg]	Decl. ^a [deg]	m_{F115W} [mag]	m_{F150W} [mag]	m_{F277W} [mag]	m_{F444W} [mag]	m_{F770W} [mag]	z_{photo}^b	$\log L_{\text{bol}}^b$ [erg s ⁻¹]	A_V^b [mag]	z_{system}	θ^c [']	
CW-B5-15958	#1	10 ^h 01 ^m 59 ^s .842	2°26′43″.35	28.2 ± 0.1	27.87 ± 0.05	26.22 ± 0.01	24.31 ± 0.01	-	7.7 ^{+0.4} _{-1.4}	46.6 ^{+0.2} _{-0.3}	2.9 ^{+0.3} _{-0.2}	7.1 ^{+0.5} _{-0.9}	0.37
	#2	10 ^h 01 ^m 59 ^s .829	2°26′43″.66	28.1 ± 0.1	28.2 ± 0.1	26.56 ± 0.01	24.78 ± 0.01	-	6.5 ^{+0.7} _{-0.8}	46.2 ^{+0.4} _{-0.3}	3.1 ^{+0.4} _{-0.3}	-	-
	EC ^d	10 ^h 01 ^m 59 ^s .849	2°26′43″.20	-	-	26.09 ± 0.08	25.80 ± 0.08	-	-	-	-	-	-
CW-A6-19978	#1	09 ^h 58 ^m 59 ^s .552	2°07′29″.32	28.13 ± 0.06	28.22 ± 0.08	27.2 ± 0.01	25.54 ± 0.01	-	6.4 ^{+0.6} _{-0.7}	45.8 ^{+0.5} _{-0.3}	3.1 ^{+0.4} _{-0.3}	6.4 ^{+0.7} _{-0.7}	0.21
	#2	09 ^h 58 ^m 59 ^s .552	2°07′29″.53	-	-	28.42 ± 0.08	26.64 ± 0.01	-	6.8 ^{+1.9} _{-1.6}	45.5 ^{+0.3} _{-0.4}	2.6 ^{+1.6} _{-0.4}	-	-
CW-B2-4383	#1	10 ^h 00 ^m 13 ^s .529	2°28′18″.77	27.66 ± 0.04	28.18 ± 0.07	27.46 ± 0.01	25.89 ± 0.01	25.42 ± 0.01	6.2 ^{+0.2} _{-0.4}	45.7 ^{+0.1} _{-0.1}	3.1 ^{+0.3} _{-0.2}	6.0 ^{+0.2} _{-0.2}	0.28
	#2	10 ^h 00 ^m 13 ^s .512	2°28′18″.68	-	-	27.8 ± 0.1	26.17 ± 0.04	26.3 ± 0.2	5.9 ^{+0.2} _{-0.4}	45.2 ^{+0.1} _{-0.2}	2.1 ^{+0.2} _{-0.2}	-	-

^a J2000 values obtained from the image-based modeling of the F277W image.

^b Derived from the SED fitting with the QSO model.

^c Projected separation derived from the image-based modeling of the F277W image.

^d Extended component around component #1.

The estimated photometric redshifts of components #1 and #2 are $z_{\text{photo}} = 7.7_{-1.4}^{+0.4}$ and $z_{\text{photo}} = 6.5_{-0.8}^{+0.7}$, respectively. The medians of the two photometric redshifts differ by $\Delta z = 1.2$, but their 68% confidence intervals overlap in the range $z_{\text{photo}} = 6.3\text{--}7.2$. Therefore, we conclude that the photometric redshifts are consistent with the two components being at the same redshift. We then combine their photometric redshift probability distribution functions (PDFs) and calculate the median and 68% confidence interval of the combine distribution as $z_{\text{photo}} = 7.1_{-0.9}^{+0.5}$, which we assign as the photometric redshift of the system z_{system} . The projected separation between the components #1 and #2 is $\theta = 0''.37$ in F277W, corresponding to $1.9_{-0.1}^{+0.2}$ kpc at z_{system} .

Interestingly, we find a $>3\sigma$ off-centered extended feature south of component #1, as shown in the positive residuals after subtracting the fitted PSF-PSF model in F277W and F444W (the bottom-right panel of Figure 3 (b)). Since no similar structure is observed in the symmetric position relative to the PSF spike structure, it is unlikely that this extended component is a PSF diffraction feature that is not perfectly removed from the foreground subtraction. To account for this extended feature in the image-based modeling, we fit component #1 with a composite model of PSF and Sérsic, while component #2 is fitted with a PSF. This composite model results in significantly lower BIC values in both F277W and F444W compared to the PSF-PSF model. The center of this extended compo-

nent has a $0''.20$ offset from component #1, which corresponds to $1.03_{-0.04}^{+0.10}$ kpc at z_{system} . Extended components around LRDs are found for other LRDs selected with the pixel-by-pixel selection method (Tanaka et al. in preparation). Recently, Chen et al. (2024) reported that four out of eight spectroscopically confirmed and less-gravitationally-lensed LRDs in UNCOVER fields show off-centered extended components. Unless coincidentally projected onto another galaxy, brown dwarfs are not expected to exhibit such extended features. Therefore, this finding further supports that CW-B5-15958-#1 is an LRD rather than a brown dwarf. This extended component might represent an underlying host galaxy disturbed by interactions (e.g., tidal tail) or an ionization cone.

We also find another separated companion detected in F115W and F150W with the separation of $0''.76$ (corresponding $3.9_{-0.2}^{+0.3}$ kpc at z_{system}) from component #1 as observed in CW-B2-4383 (section 3.3). This companion is undetected in F814W, and assuming it has a Lyman break between F814W and F115W, it is consistent with being at the same redshift. Therefore, this system is likely to consist of two LRDs, one with nearby extended components, and an additional companion galaxy located approximately 3.9 kpc away at the same redshift. To spectroscopically confirm the dual LRD (i.e., obtaining spectroscopic redshifts) and explore the nature of the off-centered extended components and the companion further, spatially resolved deep spectroscopy with

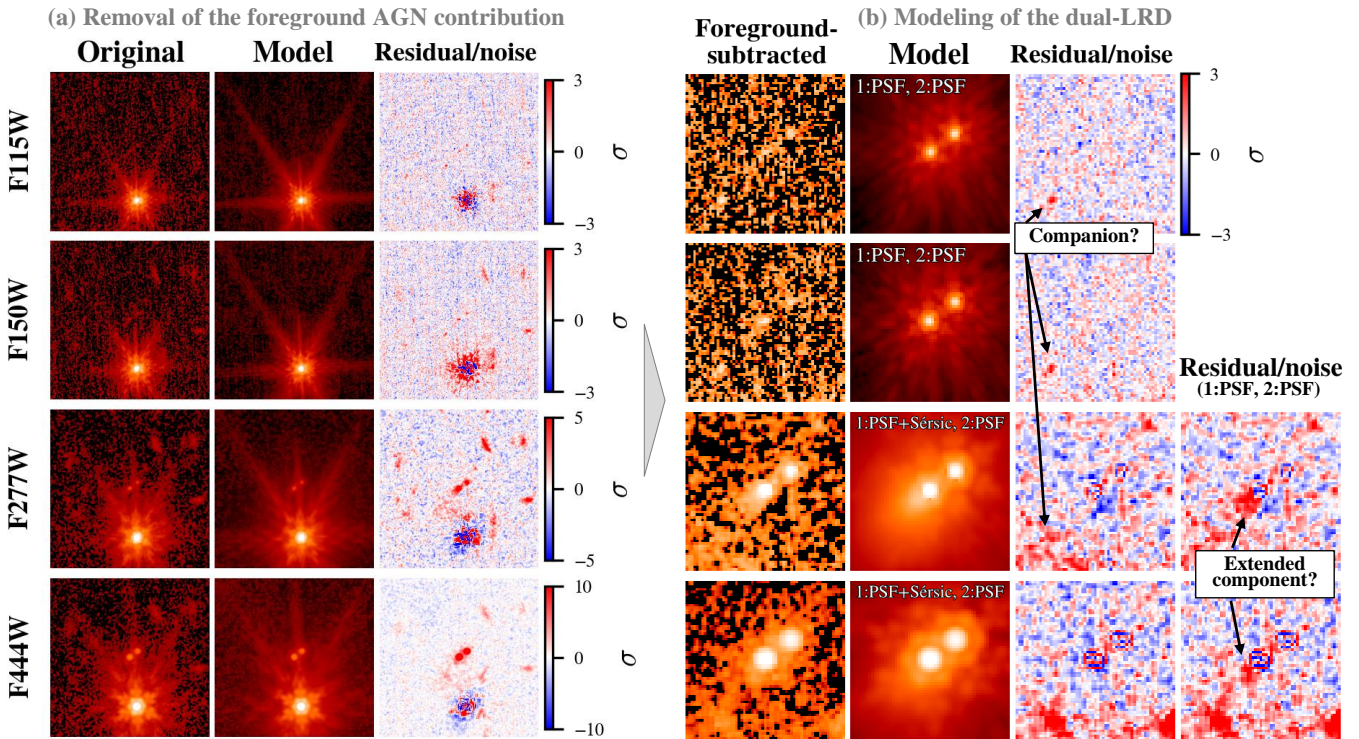


Fig. 3. The image-based modeling analysis on CW-B5-15958. (a) Modeling of CID-643 to remove the foreground contribution by its AGN and host galaxy. The left, middle, and right columns show the $6'' \times 6''$ original images, the best-fit model, and the residual (original - model) scaled by the noise map in each filter. Note that, here, the residual image is Original - CID-643 (AGN and host component), and we do not subtract the CW-B5-15958 components. (b) Modeling of CW-B5-15958 after subtracting CID-643 contribution. Same for the panels (a), but focusing on CW-B5-15958 with the image size of $1''.8 \times 1''.8$. In F277W and F444W, the best model is the composite model of double PSFs for each LRD and Sérsic for the extended component around component #1. For comparison, we also plot the scaled residual image with the PSF-PSF model (without the additional extended component).

JWST/NIRSpec IFU is essential.

3.2 CW-A6-19978

As shown in figure 1 (A), CW-A6-19978 has a fainter component #2 located to the north of component #1. Using the F277W and F444W images, CW-A6-19978 is best modeled with a single PSF for each component based on a significantly lower BIC than other models. The $m_{F277W} - m_{F444W}$ colors for components #1 and #2 are 1.7 and 1.8, respectively, and the optical slopes β_{opt} (where $F_{\lambda} \propto \lambda^{\beta}$) estimated from these two filters are $\beta_{\text{opt}} = 1.33 \pm 0.02$ and 1.56 ± 0.07 for components #1 and #2, respectively, similar to the optical slope observed in typical LRDs (Matthee et al. 2024a; Greene et al. 2024; Kocevski et al. 2024).

With the F115W and F150W images, the best-fit model has a significantly lower BIC when using only one PSF for component #1, i.e., no model for component #2. Therefore, we conclude that component #2 is undetected in F115W and F150W. Component #1 has the $m_{F115W} - m_{F150W}$ color of -0.1 , indicating a blue excess (excess in F_{λ} and flat slope in F_{ν}). SED fitting analysis with the QSO model results in the photometric redshift of component #1 and #2 as $z_{\text{photo}} = 6.4^{+0.6}_{-0.7}$ and $z_{\text{photo}} = 6.8^{+1.9}_{-1.6}$, resulting the photometric redshift of this system as $z_{\text{system}} = 6.4^{+0.7}_{-0.7}$. When fitting component #2, an upper limit on the photometry is used for the F115W and F150W bands. The separation between the components #1 and #2 is $\theta = 0''.21$ in F277W, the smallest among the three candidates in this study. The projected separation corresponds to $1.16^{+0.07}_{-0.07}$ kpc at z_{system} . In summary, both components

are well-explained as unresolved components with a similar SED (figure 1) to typical LRDs, with component #2 detected only in F277W and F444W.

3.3 CW-B2-4383

As shown in figure 1 (A), CW-B2-4383 has a fainter component #2 located to the west of component #1. A model with a PSF for component #1 and a Sérsic for component #2 has a significantly lower BIC than other model configurations for the F277W and F444W images. The best-fit Sérsic components have $r_e \sim 0''.1$ and $n \sim 0.5$ for F277W and $r_e \sim 0''.04$ and $n \sim 5$ (hitting the upper limit) for F444W with the latter suggesting a very compact morphology consistent with a PSF component. However, the F277W image cutout (figure 1) shows a slightly extended structure, which may be the result of its lower luminosity in F277W and potential contributions from extended components, as observed in CW-B5-15958 (section 3.1). The $m_{F277W} - m_{F444W}$ colors for components #1 and #2 are each 1.6, respectively. The optical slope β_{opt} estimated from F444W and F277W are $\beta_{\text{opt}} = 1.14 \pm 0.04$ and 1.08 ± 0.06 for components #1 and #2, respectively, similar to the optical slope observed in typical LRDs (Matthee et al. 2024a; Greene et al. 2024; Kocevski et al. 2024).

Similar to CW-A6-19978, a model composed of only one PSF for component #1 has a significantly lower BIC than other models for the F115W and F150W images. Thus, we conclude that component #2 is undetected in F115W and F150W. Component #1 has $m_{F115W} - m_{F150W}$ color of -0.5 , indicating a blue excess.

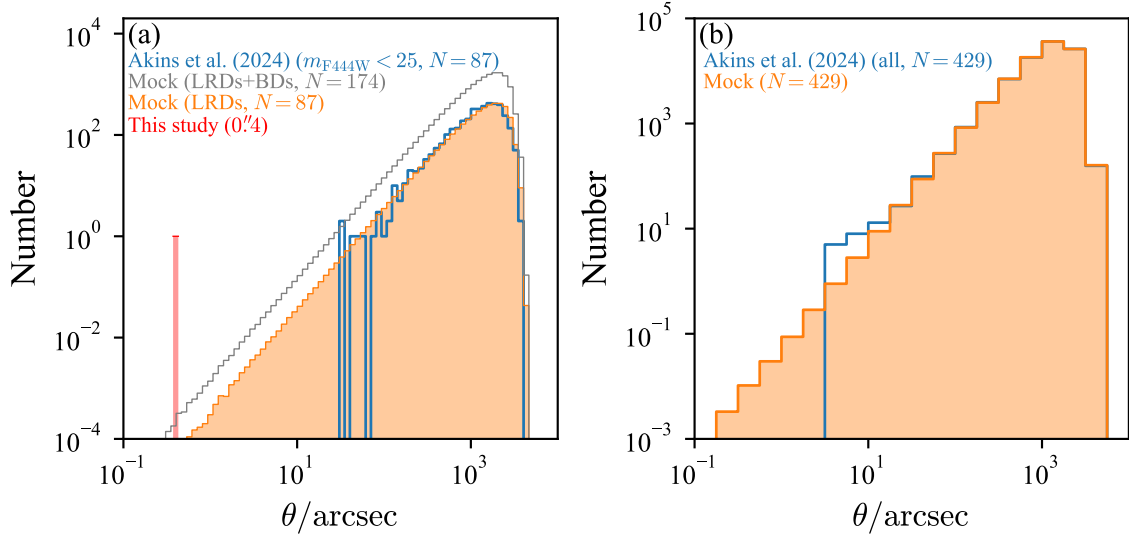


Fig. 4. Distribution of projected separation (θ) for control and mock samples. (a) Blue histogram indicates the θ distribution for a random control LRD sample ($m_{F444W} < 25$, $N = 87$). Additional histograms indicate the full mock LRD (orange; scaled to $N = 87$) and LRD+BD (gray; scaled to $N = 174$) samples generated with a random spatial distribution. The red rectangle corresponds to the detection of CW-B5-15958 at a separation of $0''.4$, which indicates the challenge to explain CW-B5-15958 as a pair of two physically unrelated objects (LRDs or BDs) at different redshifts. (b) Histograms indicate the θ distribution using the Akins et al. (2024b) LRD sample (blue; $N = 429$) and the mock LRD sample (orange; scaled to $N = 429$).

CW-B2-4383 is the only system covered by F770W among the three candidates. In this band, the PSF-PSF model yields a significantly lower BIC compared to other configurations. However, due to the limited spatial resolution of MIRI, the two components are almost entirely blended, as shown in figure 1 (b).

In addition, we find another potential companion detected in F277W and F444W as indicated in figure 1. Even with further coverage of F770W, we cannot constrain the SED and photometric redshift of this third source due to its faint photometry.

For the two brighter LRD candidates, SED fitting analysis with the QSO model results in a photometric redshift of component #1 and #2 as $z_{\text{photo}} = 6.2^{+0.2}_{-0.4}$ and $z_{\text{photo}} = 5.9^{+0.2}_{-0.4}$, resulting the photometric redshift of this system as $z_{\text{system}} = 6.0^{+0.2}_{-0.2}$. The separation between the components is $0''.28$, corresponding to the projected separation of $1.60^{+0.03}_{-0.03}$ kpc at z_{system} . For component #2, an upper limit on the photometry is used for F115W and F150W. Due to the inclusion of F770W photometry, CW-B2-4383 exhibits smaller uncertainties on z_{photo} compared to the other dual LRD candidates. However, the F770W photometry may involve substantial uncertainties, and the SED fitting with the QSO model only incorporates galaxy templates. Therefore, the uncertainties in the photometric redshifts can be underestimated.

CW-B2-4383 is also covered by ALMA in Band 3 (89.5-105.4 GHz, Project ID: 2016.1.00171.S) with a continuum sensitivity of 0.0395 mJy/beam. We do not find any detections in the continuum or signs of emission lines in the cubes. This non-detection is consistent with previous studies that have reported the absence of LRD detections in ALMA observations (Labbe et al. 2023; Akins et al. 2024b).

As mentioned in section 2, due to the S/N cut, our method can reliably select typical LRDs with high completeness for $m \lesssim 25$, i.e., our method can overlook fainter LRDs (see Tanaka et al. in preparation). Within the three LRD pairs presented here, the fainter components (#2) of CW-A6-19978 and CW-B2-4383 have $m_{F444W} = 26.64$ and 26.17, respectively, which are significantly fainter than the magnitude limit. These faint LRDs are identified

because they are located near relatively brighter LRDs (component #1), suggesting that our method overlooks faint dual LRDs. Therefore, we focus the subsequent discussion on CW-B5-19958, a solid candidate with both components (#1 and #2) being significantly brighter than our chosen magnitude limit.

4 Discussion

We present the discovery of the first three dual LRD candidates, all within the COSMOS-Web region (section 3). First, we consider that CW-B5-15958 is a valid dual LRD candidate. This entails the use of a control LRD sample to determine the probability that these LRDs can coincidentally appear close to each other on the sky (i.e., chance projection of two objects at different redshifts) with a projected separation less than that of CW-B5-15958 ($\theta \leq 0''.37$; sections 4.1 and 4.2). With a very low probability of being the result of a chance projection, as shown below, CW-B5-15958 is considered to be a dual LRD, with each component at the same redshift, which allows us to estimate the angular clustering of LRDs on small scales (section 4.3).

4.1 Probability of a chance projection of LRDs

Since both LRD components (#1 and #2) of CW-B5-15958 have $m_{F444W} < 25$ (table 1), we apply this magnitude cut to the sample from Akins et al. (2023), resulting in a control sample with a size of $N = 87$. This control sample provides a comprehensively selected set of LRDs within the COSMOS-Web region with $m_{F444W} < 25$.

Next, we select all possible pairs of two LRDs from this control sample and measure the distribution of their projected separations in the sky. In figure 4 (a), we compare this separation distribution to a mock separation distribution, which assumes the same number of objects randomly distributed within the COSMOS-Web field of view, which is simply modeled as a square region with the area of

0.54 deg². The two distributions align well, suggesting that the global distribution of LRDs can be explained by random distribution. Note that this result does not imply that LRDs do not cluster since here we use all LRDs in Akins et al. (2024b) across different redshifts to estimate the possibility that LRDs at any redshifts appear close in projection coincidentally (also see section 4.3).

We then generate a random mock sample multiple times. We use the Monte Carlo method to examine the probability of finding one LRD pair with $\theta \lesssim 0''.4$ in these distributions. Based on 100,000-iteration results, the probability of finding one LRD pair with $\theta < 0''.4$ is 0.025% (corresponding to 3.7σ). This result suggests that the dual LRD candidates are at the same redshift and are physically related as merging pairs.

4.2 Probability of being projected LRD - BD pairs

The number of BDs that can contaminate the color selection of LRDs is not significantly high. For example, Akins et al. (2024b) reported that the contamination fraction is $\sim 20\%$ and $\sim 10\%$ for NIRCcam-only selected and MIRI-detected samples from a SED fitting analysis. Greene et al. (2024) also reported the contamination (BD) fraction of $\sim 20\%$ for the NIRCcam-only selected sample from the spectroscopic follow-up observations.

Here, we construct a sample that includes both LRDs and BDs, and perform a chance projection analysis similar to section 4.1. Akins et al. (2024b) excluded BDs from the photometrically selected sample through SED fitting analysis, and therefore, our control sample derived from their sample does not include BDs. To make a sample including both LRDs and BDs, we assume a contamination fraction of 50%, which is higher than the previously reported values ($\sim 10\text{-}20\%$) for a conservative examination. With this contamination fraction, the total sample size becomes $N = 174$. Note that we do not consider the possibility of BD binary. The projected separation distribution of mock data created with the random spatial distribution is shown in figure 4 (b). Based on 100,000-iteration Monte-Carlo analysis, the probability of finding one pair with $\theta < 0''.4$ is 0.11% (corresponding to 3.3σ). From this analysis, we confirm that the probability of finding projected pairs (now including LRD-BD and BD-BD pairs) with separations of approximately $0''.4$ remains sufficiently low. While the SED fitting analysis (section 3) suggests that BD templates cannot describe the SEDs of each LRD in our dual LRD candidates, we further support this conclusion from another perspective by ruling out the possibility of chance projections.

4.3 Excess clustering on kpc scales

We assume that CW-B5-15958 is indeed a true dual LRD at $z \sim 7$ and estimate the angular auto-correlation function (angular ACF, $\omega(\theta)$). For this purpose, we generate a control sample of 80 objects at $z \sim 7$ (median $z_{\text{photo}} = 5\text{-}8$) with $m_{\text{F444W}} < 25$. Since our selection has high completeness for high- S/N sources (see Tanaka et al. in prep), we limit the magnitude range to $m_{\text{F444W}} \lesssim 25$ which does not include the other two tentative candidates, CW-A6-19978 and CW-B2-4383. The angular ACF of LRDs at $\theta \leq 0''.4$ is estimated as

$$\omega(\leq 0''.4) = \left\{ \binom{80}{2} \times \frac{\pi (0''.4)^2}{0.56 \text{ deg}^2} \right\}^{-1} - 1 = 4.6 \times 10^3. \quad (1)$$

Then, assuming that $\omega(\theta)$ follows the power law as equation (2), we transform $\omega(\leq 0''.4)$ into $\omega(0''.4)$ as $\omega(0''.4) = 2.5^{+5.8}_{-2.0} \times 10^3$, where the 68% confidence interval is estimated from Poisson statistics (Gehrels 1986).

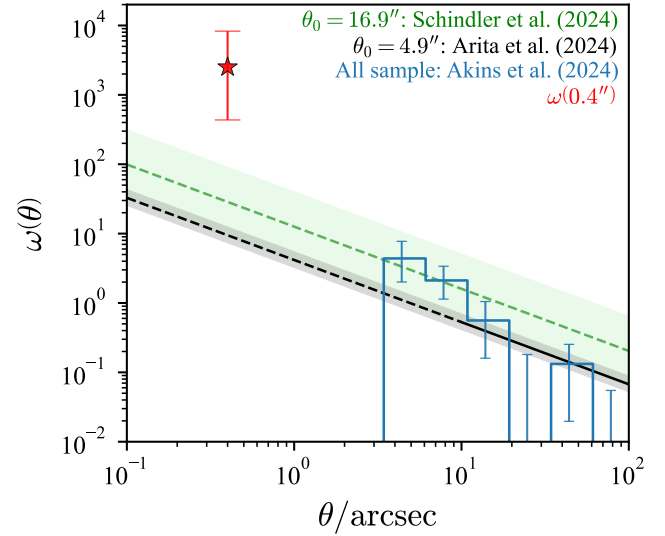


Fig. 5. Angular auto-correlation function of LRDs integrated at $z = 5\text{-}8$. The red star symbol indicates our $\omega(0''.4)$ estimate. Black/green lines and gray/green shaded regions indicate the angular auto-correlation function estimated by Arita et al. (2024)/Schindler et al. (2024). The blue histogram indicates the ACF derived from the full sample of Akins et al. (2024b).

4.3.1 Comparison with ACFs with previous estimates

Recently, studies have conducted clustering analyses of LRDs and estimated their halo mass (M_{halo} , e.g., Pizzati et al. 2024). For instance, Arita et al. (2024) conducted a clustering analysis of low-luminosity JWST-found broad-line (FWHM $\gtrsim 1000$ km/s) AGNs at $z \sim 5\text{-}6$, including LRDs, and estimate the halo mass of $\log(M_{\text{halo}}/h^{-1}M_{\odot}) = 11.46^{+0.20}_{-0.25}$, lower than the halo mass of high- z quasars ($\log(M_{\text{halo}}/h^{-1}M_{\odot}) \sim 12\text{-}13$, e.g., Shimasaku & Izumi 2019; Arita et al. 2023; Córdova Rosado et al. 2024; Eilers et al. 2024). Note that the halo mass of LRDs is still in discussion, and Schindler et al. (2024) reported a minimum halo mass of $\log(M_{\text{halo}}/h^{-1}M_{\odot}) = 12.11^{+0.72}_{-0.84}$, similar to high- z quasars. In this section, we compare the $\omega(0''.4)$ estimates with the ACFs expected from the above previous M_{halo} estimates of LRDs (and JWST-found AGNs).

For comparison, we follow Arita et al. (2024) and model $\omega(\theta)$ as

$$\omega(\theta) = \left(\frac{\theta}{\theta_0} \right)^{-\beta}, \quad (2)$$

with $\beta = 0.90$. We further assume $\log(M_{\text{halo}}/h^{-1}M_{\odot}) = 11.46^{+0.20}_{-0.25}$ as found by Arita et al. (2024). With the relation between halo mass and correlation length used in Arita et al. (2023), the correlation length is predicted to be $9.2^{+1.4}_{-1.5} h^{-1} \text{ Mpc}$. Applying Limber's equation (Limber 1953), which transforms the spatial correlation function to the angular correlation function, and consideration of the redshift distribution of LRDs at $z = 5\text{-}8$ (Akins et al. 2024b), we obtain $\theta_0 = 4''.9^{+1''.8}_{-1''.5}$. In Figure 5, we compare this value of $\omega(0''.4)$ to an extrapolation of previous estimates on larger scales and find an enhancement, $\sim 3 \times 10^2$ times higher.

In the above calculation, we assume that LRDs at different redshifts reside in similar mass halos. If we instead assume that LRDs at $z \sim 7$ are progenitors of those at $z \sim 5$ and account for halo mass evolution based on the Extended Press-Schechter theory (Bower 1991), the halo mass decreases to $\log(M_{\text{halo}}/h^{-1}M_{\odot}) = 11.26$, giving a correlation length of $7.9 h^{-1} \text{ Mpc}$ ($\theta_0 \sim 3''.6$). In this case, the $\omega(0''.4)$ excess from the extrapolated value ($\sim 4 \times 10^2$) would

be even higher compared to the non-evolution scenario. Even if we assume a large halo mass of $\log(M_{\text{halo}}/h^{-1}M_{\odot}) = 12.11^{+0.72}_{-0.84}$ estimated from Schindler et al. (2024), the correlation length is $\sim 16.5^{+13.9}_{-7.5} h^{-1}\text{Mpc}$ ($\theta_0 \sim 16''.9^{+44.5}_{-12.2}$). In this case, the $\omega(0''.4)$ is still $\sim 9 \times 10$ times higher than the extrapolated value.

The correlation function by Arita et al. (2024) is based on the measurements of JWST AGNs, including not only LRDs but also other JWST AGNs; thus, there is a possibility that it is not a pure comparison if LRDs and non-LRD AGNs reside in halos of different mass range. The θ range in Arita et al. (2024) is $\theta = 10\text{-}100''$ dominated by the two-halo term, far from $\theta \sim 0''.4$ dominated by the one-halo term. Therefore, it will be essential to place constraints on the ACF of LRDs from a large-scale to kpc-scale in future observations covering large areas with JWST/NIRCam WFSS, such as COSMOS-3D and NEXUS (Shen et al. 2024; Zhuang et al. 2024).

If the ACF excess is special for LRDs, one possible interpretation is that LRDs are AGNs. Such an excess in the ACF at small θ is qualitatively consistent with AGNs at lower redshifts (e.g., Hennawi et al. 2006; Eftekharzadeh et al. 2017; Bhowmick et al. 2019; Shen et al. 2023; Comerford et al. 2024), which may indicate that LRDs are AGNs and that close interactions trigger their activity. However, normal galaxies also have excess ACFs on small scales. Therefore, to compare with LRDs, we need to constrain the ACF of normal galaxies at the same redshifts as well.

4.3.2 Comparison with all LRDs in Akins et al. (2024b)

As shown in figure 4, the number of pairs decreases with smaller θ . Thus, bridging the gap between the scales explored in previous studies (e.g., $\theta = 10''\text{-}100''$ in Arita et al. 2024) and this work ($\theta = 0''.4$) requires a larger LRD sample.

In this section, we utilize the largest LRD sample to date from Akins et al. (2024b), consisting of 429 LRDs photometrically selected from COSMOS-Web to constrain the small-scale ACF. The redshift range for this sample is $z_{\text{photo}} \sim 5\text{-}8$. The projected separation (θ) distribution of this sample is shown in figure 4 (b).

We make 42,900 (100 times the number of LRDs) random points over the COSMOS-Web region. Then, following the method of Arita et al. (2024), we evaluate the angular ACF using the estimator from Landy & Szalay (1993);

$$\omega(\theta) = \frac{LL(\theta) - 2LR(\theta) + RR(\theta)}{RR(\theta)}, \quad (3)$$

where $LL(\theta)$, $LR(\theta)$, and $RR(\theta)$ represent the normalized pair counts of LRDs - LRDs, LRDs - random points, and random points - random points within the θ range. For simplicity, we ignore the integral constraints. The errors are estimated assuming Poisson statistics. The resulting ACF, shown in blue plots in figure 5, generally aligns with the prediction from Arita et al. (2024). Over 68% confidence intervals, the angular ACF has a slight excess at $\theta \lesssim 10''$ from the expectation of Arita et al. (2024).

As discussed in sections 2 and 3, our selection method overlooks fainter LRDs with $m_{F444W} \gtrsim 25$ compared to Akins et al. (2024b). Consequently, $\omega(0''.4)$ is derived only from bright sources with $m_{F444W} = 24.3$ and 24.8 , which are among the brighter objects in the Akins et al. (2024b) sample ($m \lesssim 27$). Here, we assume that the ACF does not strongly depend on magnitude (e.g., Shen et al. 2009; Croom et al. 2005) and directly compare $\omega(0''.4)$ with the ACF derived from the entire Akins et al. (2024b) sample without applying a magnitude cut. The ACF excess at $\theta = 0''.4$ from the power-law given by equation (2) is significantly larger than the excess at $\theta = 4''\text{-}10''$.

Interestingly, even when using the full sample from Akins et al.

(2024b), we do not find any pairs with $\theta = 0''.4\text{-}3''.8$. For $\theta \gtrsim 0''.5$, the influence of a companion LRD on compactness measurements should be negligible, meaning LRDs with a $\theta \sim 1''$ companion should be detectable with typical selection methods. This absence may suggest that the triggering of LRD activity through interactions works only on very small scales ($\sim 0''.4$), corresponding to 1.9-2.5 kpc at $z = 5\text{-}8$. Considering that LRDs may have low stellar masses such as $M_* \lesssim 10^9 M_{\odot}$ (Chen et al. 2024) or $M_* \sim 5 \times 10^7 M_{\odot}$ (Matthee et al. 2024b), the spatial scale at which AGN activity is triggered by interactions in LRDs may be smaller than that for typical low- z AGNs. Expanding survey fields and performing spectroscopic identification of LRDs are crucial for constructing a larger sample and understanding their clustering and interaction-driven triggering.

Finally, all analyses here are based on candidates of dual LRDs without spectroscopic confirmations; thus, further spectroscopic identification is crucial to verify the arguments. The sample size of candidates is still, at most, only three, and it is needed to create a more statistically significant sample from a large NIRCam imaging data (e.g., Morishita et al. 2024).

5 Conclusion

By applying the pixel-by-pixel color selection method to the COSMOS-Web imaging data, we identify the first three dual LRD candidates (figure 1). In all candidates, LRD candidates have a color satisfying color selection threshold, $m_{F277W} - m_{F444W} > 1.5$. Through image-based modeling (figure 3), we constrain the photometry and morphology of each component. Then, we estimate their photometric redshifts from SED fitting. The key results are as follows:

- In the most solid and brightest candidate, CW-B5-15958 (section 3.2), both components #1 and #2 are bright with $m_{F444W} = 24.3$ and 24.8 and are detected across all available NIRCam filters (F115W, F150W, F277W, and F444W). Their SEDs show clear V-shaps and exclude the possibility that these red objects are Galactic BDs. The photometric redshift of this system is $z_{\text{system}} = 7.1^{+0.5}_{-0.9}$ based on that of component #1 ($z_{\text{photo}} = 7.7^{+0.4}_{-1.4}$) and component #2 ($z_{\text{photo}} = 6.5^{+0.7}_{-0.8}$). Their projected separation of $0''.37$ corresponds to $1.9^{+0.2}_{-0.1}$ kpc at z_{system} . Additionally, we detect an off-centered extended component located $0''.20$ (1.0 kpc) away from component #1 and a separated companion $0''.76$ (3.9 kpc) away from component #1.
- For the other two candidates, CW-A6-19978 (section 3.2) and CW-B2-4383 (section 3.3), component #1 shows clear V-shape SED. Component #2 of both systems is faint and undetected in F115W and F150W. In CW-B2-4383, component #2 is better fitted by a Sérsic component in F277W and F444W. From these characteristics, we conclude that these two are tentative dual LRDs candidates.
- Based on the projected separation (θ) distribution analysis of the control and mock samples, the likelihood of these candidates being chance projections of physically unrelated LRDs or BDs at different redshifts is very low (figure 4).
- If these candidates are indeed pairs at the same redshifts, our results suggest that LRDs show excess ($\sim 3 \times 10^2$ times) clustering on kpc scales (figure 5) from extrapolation of a power-law ACF of JWST-found AGNs measured over $10''\text{-}100''$. Given that we cannot find any LRD pairs with $\theta = 0''.4\text{-}3''.8$, the excess clustering may indicate that these LRDs are AGNs triggered through interactions only in kpc separations (also see the

Appendix).

If we assume that LRDs are AGNs, these dual LRD candidates could be the highest-redshift dual AGNs discovered to date (c.f., Übler et al. (2024) and Matsuoka et al. (2024) reported dual AGNs at $z = 7.15$ and $z = 6.05$, respectively). However, all three candidates are photometrically selected without spectroscopic confirmation. Therefore, spectroscopic follow-up observations are essential to confirm whether they are dual LRDs and constrain the statistics about dual LRDs (e.g., dual fractions). Moreover, since the current sample size is small, we need to expand the sample further with large field surveys. Investigating the environments of LRDs with larger spectroscopic samples and comparing them to other AGNs and galaxies will also be critical for understanding their nature.

Acknowledgments

We thank Khee-Gan Lee for the fruitful discussion. This work is based on observations made with the NASA/ESA/CSA James Webb Space Telescope. The data were obtained from the Mikulski Archive for Space Telescopes at the Space Telescope Science Institute, which is operated by the Association of Universities for Research in Astronomy, Inc., under NASA contract NAS 5-03127 for JWST. These observations are associated with program IDs 1727. Numerical computations were in part carried out on the iDark cluster, Kavli IPMU. This work was made possible by utilising the CANDIDE cluster at the Institut d'Astrophysique de Paris. The cluster was funded through grants from the PNCG, CNES, DIM-ACAV, the Euclid Consortium, and the Danish National Research Foundation Cosmic Dawn Center (DNRF140). It is maintained by Stephane Rouberol.

Funding

Kavli IPMU is supported by World Premier International Research Center Initiative (WPI), MEXT, Japan. Takumi S. Tanaka is supported by Forefront Physics and Mathematics Program to Drive Transformation (FoPM), a World-leading Innovative Graduate Study (WINGS) Program, the University of Tokyo. John D. Silverman is supported by JSPS KAKENHI (JP22H01262) and the World Premier International Research Center Initiative (WPI), MEXT, Japan. Junya Arita is supported by the Japan Society for the Promotion of Science (JSPS) KAKENHI Grant Number JP24KJ0858. Kohei Inayoshi acknowledges support from the National Natural Science Foundation of China (12073003, 12003003, 11721303, 11991052, 11950410493), and the China Manned Space Project (CMSCST-2021-A04 and CMS-CSST-2021-A06). Makoto Ando is supported by the Data-Scientist-Type Researcher Training Project of The Graduate University for Advanced Studies, SOKENDAI.

References

Akins, H. B., Casey, C. M., Allen, N., et al. 2023. *ApJ*, 956, 61
 Akins, H. B., Casey, C. M., Berg, D. A., et al. 2024a. *arXiv e-prints*, arXiv:2410.00949
 Akins, H. B., Casey, C. M., Lambrides, E., et al. 2024b. *arXiv e-prints*, arXiv:2406.10341
 Alexander, T., & Natarajan, P. 2014. *Science*, 345, 1330–1333
 Alonso, M. S., Lambas, D. G., Tissera, P., & Coldwell, G. 2007. *MNRAS*, 375, 1017–1024
 Amaro-Seoane, P., Audley, H., Babak, S., et al. 2017. *arXiv e-prints*, arXiv:1702.00786

Ananna, T. T., Bogdán, Á., Kovács, O. E., Natarajan, P., & Hickox, R. C. 2024. *arXiv e-prints*, arXiv:2404.19010
 Arita, J., Kashikawa, N., Matsuoka, Y., et al. 2023. *ApJ*, 954, 210
 Arita, J., Kashikawa, N., Onoue, M., et al. 2024. *arXiv e-prints*, arXiv:2410.08707
 Barausse, E., Dvorkin, I., Tremmel, M., Volonteri, M., & Bonetti, M. 2020. *ApJ*, 904, 16
 Barro, G., Pérez-González, P. G., Kocevski, D. D., et al. 2024. *ApJ*, 963, 128
 Begelman, M. C., Volonteri, M., & Rees, M. J. 2006. *MNRAS*, 370, 289–298
 Beifiori, A., Courteau, S., Corsini, E. M., & Zhu, Y. 2012. *MNRAS*, 419, 2497–2528
 Bertin, E. In Evans, I. N., Accomazzi, A., Mink, D. J., & Rots, A. H., editors, *Astronomical Data Analysis Software and Systems XX*, volume 442 of *Astronomical Society of the Pacific Conference Series*, page 435, 2011
 Bertin, E., & Arnouts, S. 1996. *A&AS*, 117, 393–404
 Bhowmick, A. K., DiMatteo, T., Eftekharzadeh, S., & Myers, A. D. 2019. *MNRAS*, 485, 2026–2040
 Bhowmick, A. K., Blecha, L., Ni, Y., et al. 2022. *MNRAS*, 516, 138–157
 Bickley, R. W., Ellison, S. L., Salvato, M., et al. 2024. *MNRAS*, 533, 3068–3089
 Bogdán, Á., Goulding, A. D., Natarajan, P., et al. 2024. *Nature Astronomy*, 8, 126–133
 Bouchet, P., García-Marín, M., Lagage, P. O., et al. 2015. *PASP*, 127, 612
 Bower, R. G. 1991. *MNRAS*, 248, 332–352
 Bromm, V., & Loeb, A. 2003. *ApJ*, 596, 34–46
 Bushouse, H., Eisenhamer, J., Dencheva, N., et al., 2023
 Byrne-Mamahit, S., Patton, D. R., Ellison, S. L., et al. 2024. *MNRAS*, 528, 5864–5879
 Capelo, P. R., Volonteri, M., Dotti, M., et al. 2015. *MNRAS*, 447, 2123–2143
 Casey, C. M., Kartaltepe, J. S., Drakos, N. E., et al. 2023. *ApJ*, 954, 31
 Casey, C. M., Akins, H. B., Kokorev, V., et al. 2024. *ApJL*, 975, L4
 Chen, C.-H., Ho, L. C., Li, R., & Zhuang, M.-Y. 2024. *arXiv e-prints*, arXiv:2411.04446
 Chen, N., Di Matteo, T., Ni, Y., et al. 2023. *MNRAS*, 522, 1895–1913
 Comerford, J. M., Nevin, R., Negus, J., et al. 2024. *ApJ*, 963, 53
 Córdova Rosado, R., Goulding, A. D., Greene, J. E., et al. 2024. *arXiv e-prints*, arXiv:2410.24020
 Croom, S. M., Boyle, B. J., Shanks, T., et al. 2005. *MNRAS*, 356, 415–438
 De Rosa, A., Vignali, C., Bogdanović, T., et al. 2019. *New Astronomy Reviews*, 86, 101525
 DeGraf, C., Di Matteo, T., Treu, T., et al. 2015. *MNRAS*, 454, 913–932
 Di Matteo, T., Colberg, J., Springel, V., Hernquist, L., & Sijacki, D. 2008. *ApJ*, 676, 33–53
 Ding, X., Silverman, J., Treu, T., et al. 2020. *The Astrophysical Journal*, 888, 37
 Eftekharzadeh, S., Myers, A. D., Hennawi, J. F., et al. 2017. *MNRAS*, 468, 77–90
 Eilers, A.-C., Mackenzie, R., Pizzati, E., et al. 2024. *ApJ*, 974, 275
 Ellison, S. L., Patton, D. R., Mendel, J. T., & Scudder, J. M. 2011. *MNRAS*, 418, 2043–2053
 Ellison, S. L., Viswanathan, A., Patton, D. R., et al. 2019. *MNRAS*, 487, 2491–2504
 Ellison, S. L., Ferreira, L., Bickley, R., et al. 2024. *arXiv e-prints*, arXiv:2412.02804
 Fabian, A. C. 2012. *ARA&A*, 50, 455–489
 Ferrarese, L., & Merritt, D. 2000. *ApJL*, 539, L9–L12
 Furtak, L. J., Zitrin, A., Plat, A., et al. 2023. *ApJ*, 952, 142
 Furtak, L. J., Labbé, I., Zitrin, A., et al. 2024. *Nature*, 628, 57
 Gehrels, N. 1986. *ApJ*, 303, 336
 Gentile, F., Casey, C. M., Akins, H. B., et al. 2024. *ApJL*, 973, L2
 Goulding, A. D., Greene, J. E., Bezanson, R., et al. 2018. *PASJ*, 70, S37
 Goulding, A. D., Pardo, K., Greene, J. E., et al. 2019. *ApJL*, 879, L21
 Graham, A. W., Onken, C. A., Athanassoula, E., & Combes, F. 2011. *MNRAS*, 412, 2211–2228
 Greene, J. E., Labbe, I., Goulding, A. D., et al. 2024. *ApJ*, 964, 39
 Gültekin, K., Richstone, D. O., Gebhardt, K., et al. 2009. *ApJ*, 698, 198–221
 Haehnelt, M. G., & Rees, M. J. 1993. *MNRAS*, 263, 168–178

- Harikane, Y., Zhang, Y., Nakajima, K., et al. 2023. *ApJ*, 959, 39
- Harikane, Y., Inoue, A. K., Ellis, R. S., et al. 2024. *arXiv e-prints*, arXiv:2406.18352
- Häring, N., & Rix, H.-W. 2004. *ApJL*, 604, L89–L92
- Harrison, C. M. 2017. *Nature Astronomy*, 1, 0165
- Hennawi, J. F., Strauss, M. A., Oguri, M., et al. 2006. *AJ*, 131, 1–23
- Hopkins, P. F., Hernquist, L., Cox, T. J., & Kereš, D. 2008. *ApJS*, 175, 356–389
- Inayoshi, K., & Maiolino, R. 2024. *arXiv e-prints*, arXiv:2409.07805
- Inayoshi, K., Kimura, S., & Noda, H. 2024. *arXiv e-prints*, arXiv:2412.03653
- Ishikawa, Y., Zakamska, N. L., Shen, Y., et al. 2024. *arXiv e-prints*, arXiv:2403.08098
- Kocevski, D. D., Onoue, M., Inayoshi, K., et al. 2023. *ApJL*, 954, L4
- Kocevski, D. D., Finkelstein, S. L., Barro, G., et al. 2024. *arXiv e-prints*, arXiv:2404.03576
- Koekemoer, A. M., Aussel, H., Calzetti, D., et al. 2007. *ApJS*, 172, 196–202
- Kokorev, V., Fujimoto, S., Labbe, I., et al. 2023. *ApJL*, 957, L7
- Kokorev, V., Caputi, K. I., Greene, J. E., et al. 2024. *ApJ*, 968, 38
- Kokubo, M., & Harikane, Y. 2024. *arXiv e-prints*, arXiv:2407.04777
- Kormendy, J., & Ho, L. C. 2013. *ARA&A*, 51, 511–653
- Koss, M., Mushotzky, R., Veilleux, S., & Winter, L. 2010. *ApJL*, 716, L125–L130
- Kroupa, P. 2001. *MNRAS*, 322, 231–246
- La Marca, A., Margalef-Bentabol, B., Wang, L., et al. 2024. *A&A*, 690, A326
- Labbe, I., Greene, J. E., Bezanson, R., et al. 2023. *arXiv e-prints*, arXiv:2306.07320
- Labbé, I., van Dokkum, P., Nelson, E., et al. 2023. *Nature*, 616, 266–269
- Lambrides, E., Garofali, K., Larson, R., et al. 2024. *arXiv e-prints*, arXiv:2409.13047
- Landy, S. D., & Szalay, A. S. 1993. *ApJ*, 412, 64
- Li, J., Zhuang, M.-Y., Shen, Y., et al. 2024
- Limber, D. N. 1953. *ApJ*, 117, 134
- Liu, H., & Inayoshi, K. 2024. *arXiv e-prints*, arXiv:2409.18194
- Loeb, A., & Rasio, F. A. 1994. *ApJ*, 432, 52
- Magorrian, J., Tremaine, S., Richstone, D., et al. 1998. *AJ*, 115, 2285–2305
- Maiolino, R., Scholtz, J., Curtis-Lake, E., et al. 2023a. *arXiv e-prints*, arXiv:2308.01230
- Maiolino, R., Uebler, H., Perna, M., et al. 2023b. *arXiv e-prints*, arXiv:2306.00953
- Maiolino, R., Risaliti, G., Signorini, M., et al. 2024. *arXiv e-prints*, arXiv:2405.00504
- Marconi, A., & Hunt, L. K. 2003. *ApJL*, 589, L21–L24
- Marley, M. S., Saumon, D., Visscher, C., et al. 2021. *ApJ*, 920, 85
- Matsuoka, Y., Onoue, M., Kashikawa, N., et al. 2016. *ApJ*, 828, 26
- Matsuoka, Y., Izumi, T., Onoue, M., et al. 2024. *ApJL*, 965, L4
- Matthee, J., Naidu, R. P., Brammer, G., et al. 2024a. *ApJ*, 963, 129
- Matthee, J., Naidu, R. P., Kotiwale, G., et al. 2024b. *arXiv e-prints*, arXiv:2412.02846
- Mazzolari, G., Gilli, R., Maiolino, R., et al. 2024. *arXiv e-prints*, arXiv:2412.04224
- Meisner, A. M., Schneider, A. C., Burgasser, A. J., et al. 2021. *ApJ*, 915, 120
- Morishita, T., Mason, C. A., Kreilgaard, K. C., et al. 2024. *arXiv e-prints*, arXiv:2412.04211
- Morley, C. V., Mukherjee, S., Marley, M. S., et al. 2024. *ApJ*, 975, 59
- Mukherjee, S., Fortney, J. J., Morley, C. V., et al. 2024. *ApJ*, 963, 73
- Niida, M., Nagao, T., Ikeda, H., et al. 2020. *ApJ*, 904, 89
- Oke, J. B., & Gunn, J. E. 1983. *ApJ*, 266, 713–717
- Omukai, K., Schneider, R., & Haiman, Z. 2008. *ApJ*, 686, 801–814
- Onoue, M., Inayoshi, K., Ding, X., et al. 2023. *ApJL*, 942, L17
- Pérez-González, P. G., Barro, G., Rieke, G. H., et al. 2024. *arXiv e-prints*, arXiv:2401.08782
- Perger, K., Fogasy, J., Frey, S., & Gabányi, K. É. 2024. *arXiv e-prints*, arXiv:2411.19518
- Perna, M., Arribas, S., Lamperti, I., et al. 2023a. *arXiv e-prints*, arXiv:2310.03067
- Perna, M., Arribas, S., Marshall, M., et al. 2023b. *A&A*, 679, A89
- Pizzati, E., Hennawi, J. F., Schaye, J., et al. 2024. *arXiv e-prints*, arXiv:2409.18208
- Reines, A. E., & Volonteri, M. 2015. *ApJ*, 813, 82
- Rieke, M. J., Kelly, D. M., Misselt, K., et al. 2023. *Publications of the Astronomical Society of the Pacific*, 135
- Schindler, J.-T., Hennawi, J. F., Davies, F. B., et al. 2024. *arXiv e-prints*, arXiv:2411.11534
- Scholtz, J., Maiolino, R., D’Eugenio, F., et al. 2023. *arXiv e-prints*, arXiv:2311.18731
- Sérsic, J. L. 1963. *Boletín de la Asociación Argentina de Astronomía La Plata Argentina*, 6, 41–43
- Shen, Y., Strauss, M. A., Ross, N. P., et al. 2009. *ApJ*, 697, 1656–1673
- Shen, Y., Hwang, H.-C., Oguri, M., et al. 2023. *ApJ*, 943, 38
- Shen, Y., Zhuang, M.-Y., Li, J., et al. 2024. *arXiv e-prints*, arXiv:2408.12713
- Shimasaku, K., & Izumi, T. 2019. *ApJL*, 872, L29
- Silverman, J. D., Kampczyk, P., Jahnke, K., et al. 2011. *ApJ*, 743, 2
- Springel, V., Di Matteo, T., & Hernquist, L. 2005. *MNRAS*, 361, 776–794
- Steffen, J. L., Fu, H., Brownstein, J. R., et al. 2023. *ApJ*, 942, 107
- Sérsic, J. L. *Atlas de Galaxias Australes*. 1968
- Tanaka, T. S., Silverman, J. D., Nakazato, Y., et al. 2024. *arXiv e-prints*, arXiv:2410.00104
- Tee, W. L., Fan, X., Wang, F., & Yang, J. 2024. *arXiv e-prints*, arXiv:2412.05242
- Temple, M. J., Hewett, P. C., & Banerji, M. 2021. *MNRAS*, 508, 737–754
- Tripodi, R., Martis, N., Markov, V., et al. 2024. *arXiv e-prints*, arXiv:2412.04983
- Übler, H., Maiolino, R., Pérez-González, P. G., et al. 2024. *MNRAS*, 531, 355–365
- Uematsu, R., Ueda, Y., Alexander, D. M., et al. 2024. *arXiv e-prints*, arXiv:2412.09737
- Volonteri, M., Pfister, H., Beckmann, R., et al. 2022. *MNRAS*, 514, 640–656
- Weston, M. E., McIntosh, D. H., Brodwin, M., et al. 2017. *MNRAS*, 464, 3882–3906
- Woods, D. F., & Geller, M. J. 2007. *AJ*, 134, 527–540
- Yu, Q., & Tremaine, S. 2002. *MNRAS*, 335, 965–976
- Yue, M., Eilers, A.-C., Annana, T. T., et al. 2024. *arXiv e-prints*, arXiv:2404.13290
- Zamora, S., Venturi, G., Carniani, S., et al. 2024. *arXiv e-prints*, arXiv:2412.02751
- Zhang, Z., Jiang, L., Liu, W., & Ho, L. C. 2024. *arXiv e-prints*, arXiv:2411.02729
- Zhu, Q., Li, Y., Li, Y., et al. 2022. *MNRAS*, 514, 5583–5606
- Zhuang, M.-Y., Wang, F., Sun, F., et al. 2024. *arXiv e-prints*, arXiv:2411.06372